

# A highly accurate perfectly-matched-layer boundary integral equation solver for acoustic layered-medium problems

Wangtao Lu<sup>\*</sup>, Liwei Xu<sup>†</sup>, Tao Yin<sup>‡</sup>, Lu Zhang<sup>§</sup>

## Abstract

Based on the perfectly matched layer (PML) technique, this paper develops a high-accuracy boundary integral equation (BIE) solver for acoustic scattering problems in locally defected layered media in both two and three dimensions. The original scattering problem is truncated onto a bounded domain by the PML. Assuming the vanishing of the scattered field on the PML boundary, we derive BIEs on local defects only in terms of using PML-transformed free-space Green's function, and the four standard integral operators: single-layer, double-layer, transpose of double-layer, and hyper-singular boundary integral operators. The hyper-singular integral operator is transformed into a combination of weakly-singular integral operators and tangential derivatives. We develop a high-order Chebyshev-based rectangular-polar singular-integration solver to discretize all weakly-singular integrals. Numerical experiments for both two- and three-dimensional problems are carried out to demonstrate the accuracy and efficiency of the proposed solver.

**Keywords:** Acoustic scattering, half-space, boundary integral equation, perfectly matched layer

## 1 Introduction

The scattering problems in a locally perturbed half-space have attracted much attention of engineers and mathematicians for many years, which arise from various applications, such as modeling acoustic and electromagnetic wave propagation over outdoor ground and sea surface, optical scattering from the surface of materials in near-field optics or nano-optics, underwater detection [18]. For unbounded exterior domain problems, the boundary integral equation (BIE) method discretizes boundaries only, reducing the problem dimension by one, and automatically satisfies the outgoing radiation condition. Therefore, it has been widely used for various scattering problems [5, 6, 8, 13, 17, 20, 22, 31, 39, 41, 44, 45].

In the literature, existing BIE solvers for layered-medium scattering problems can be classified into two approaches. First approach uses the background Green's functions [15, 35, 36] to build up the governing BIEs. They are defined only on the bounded perturbed part of the scattering surface so that no truncation is required further. Nevertheless, background Green's functions involve sophisticated Sommerfeld integrals and how to effectively evaluate them becomes the key ingredient of this approach. The second approach uses the free-space Green functions instead and then the resulting BIEs are established on the unbounded scattering surface. Special treatments are required to truncate the unbounded surface. They include the approximate truncation method [33, 37], the taper function method [34, 38, 46], and the windowed Green function method [7, 10–12, 14]. It is worth noting that among these methods, the windowed Green function method is the only high-accuracy method and enjoys a super-algebraically

---

<sup>\*</sup>School of Mathematical Sciences, Zhejiang University, Hangzhou, Zhejiang 310027, China. Email: wangtaolu@zju.edu.cn

<sup>†</sup>School of Mathematical Sciences, University of Electronic Science and Technology of China, Chengdu, Sichuan 611731, China. Email: xul@uestc.edu.cn

<sup>‡</sup>LSEC, Institute of Computational Mathematics and Scientific/Engineering Computing, Academy of Mathematics and Systems Science, Chinese Academy of Sciences, Beijing 100190, China. Email: yintao@lsec.cc.ac.cn

<sup>§</sup>School of Mathematical Sciences, University of Electronic Science and Technology of China, Chengdu, Sichuan 611731, China. Email: luzhang@std.uestc.edu.cn

convergence rate. It introduces a correction that smoothly merges the unknown functions in the original integral equations with the corresponding scattered solutions for the unperturbed flat surface, thus providing uniformly fast convergence for all incident angles as the support of the windowing function grows. However, for point-source incidences, this method needs to deal with multiple spherical-wave incidences from the expansion of the incident fields.

In a recent work [30], a PML-based BIE method was proposed for solving a two-layer wave scattering problem in two-dimensions. Similar to the second approach mentioned above, it builds up governing BIEs on an unbounded scattering surface but uses PML-transformed free-space Green's functions instead. Due to the outgoing behavior of the scattered field, waves along the unbounded surface decay exponentially inside the PML. Directly truncating the unbounded surface produces numerical solutions converging exponentially fast with the PML absorbing powers. This high-accuracy method has so far been successfully extended to more complicated structures, such as step-like scattering surfaces [28], anisotropic media [23], and locally perturbed periodic structures [42].

The present paper develops a new PML-based BIE solver, significantly improving the original one from two aspects. First, the original PML-based BIE method uses only the single-layer and double-layer operators, leading to a first-kind Fredholm system. The new method uses two extra operators: the transpose of double-layer operator and the hyper-singular operator to establish second-kind Fredholm systems. Second, Alpert's high-order quadrature rule [1], utilized by [30] in discretizing the integral operators, has not been extended to three dimensions yet. We transform the hyper-singular integral operator into weakly-singular operators and their tangential derivatives. Then, a Chebyshev-based rectangular-polar integral solver is utilized to discretize all weakly-singular integral operators for both two and three dimensions. The tangential derivatives are then obtained by directly differentiating the corresponding truncated Chebyshev expansions. Numerical examples demonstrate that, typically, we only need to set the PML thickness to twice the wavelength to obtain high accuracy and fast convergence for two- and three-dimensional scattering problems.

This paper is organized as follows. In Section 2, we describe the acoustic half-space scattering problems under Dirichlet and Neumann boundary conditions, and present corresponding BIEs based on the free-space Green function. Section 3 presents the PML-based BIEs for solving Dirichlet and Neumann problems. In Section 4.1, we derive the regularized formulations for two- and three-dimensional hyper-singular BIEs. A high order discretization method for the BIEs is proposed in Section 4.2. Section 4.3 extends the new PML-based BIE solver to layered-medium scattering problems. A variety of numerical examples in two and three dimensions are presented in Section 5 to illustrate the performance of our method.

## 2 Preliminaries

### 2.1 Half-space scattering problems

This section is devoted to an efficient and highly accurate boundary integral solver for the acoustic half-space problems. To simplify the presentation, we consider the acoustic scattering by a combination of impenetrable bounded obstacles and an infinite flat surface which may consist of some local defects. An extension of the solver to more complicated structures shall be discussed in Section 4.3.

As shown in Fig. 1,  $\Omega \in \mathbb{R}^d$ ,  $d = 2, 3$  denotes an unbounded connect open domain such that there exists constants  $f_- < f_+$  with

$$U_{f_+} \subset \Omega \subset U_{f_-}, \quad U_{f_{\pm}} := \{x = (x_1, \dots, x_d) \in \mathbb{R}^d : x_d > f_{\pm}\}.$$

The boundary  $\Gamma := \partial\Omega$  contains two parts: the unbounded flat surface

$$\Pi := \{x \in \mathbb{R}^d : x_d = 0\}$$

with some local defects and the boundary  $\partial U_0$  of a bounded obstacle  $U_0$ . Let  $u^{\text{inc}}$  be a time-harmonic incident field which is a plane pressure wave:

$$u^{\text{inc}}(x) = \exp(ikx \cdot d^{\text{inc}}), \quad x \in \mathbb{R}^d, \quad (2.1)$$

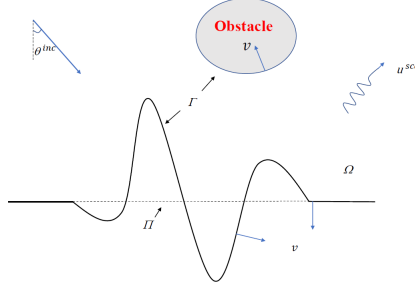


Figure 1: Problems of scattering by a locally perturbed half-space.

or a point source located at  $z \in \Omega$ :

$$u^{\text{inc}}(x) = G(x, z) := \begin{cases} \frac{i}{4} H_0^{(1)}(k|x-z|), & d = 2, \\ \frac{\exp(ik|x-z|)}{4\pi|x-z|}, & d = 3, \end{cases} \quad x \in \mathbb{R}^d, x \neq z, \quad (2.2)$$

where  $k > 0$  denotes the angular frequency,  $H_0^{(1)}$  is the first-kind Hankel function of order zero and the incident direction

$$d^{\text{inc}} = \begin{pmatrix} \sin \theta^{\text{inc}} \\ -\cos \theta^{\text{inc}} \end{pmatrix} \quad \text{in 2D} \quad \text{and} \quad d^{\text{inc}} = \begin{pmatrix} \sin \theta^{\text{inc}} \cos \phi^{\text{inc}} \\ \sin \theta^{\text{inc}} \sin \phi^{\text{inc}} \\ -\cos \theta^{\text{inc}} \end{pmatrix} \quad \text{in 3D},$$

with  $\theta^{\text{inc}}$  and  $(\theta^{\text{inc}}, \phi^{\text{inc}})$  being the incident angle and angle pair, respectively.

The scattered field  $u^{\text{sca}}$  satisfies the Helmholtz equation

$$\Delta u^{\text{sca}} + k^2 u^{\text{sca}} = 0. \quad (2.3)$$

For simplicity, on the boundary  $\Gamma$ , we impose the Dirichlet boundary condition

$$u^{\text{sca}} = f( := -u^{\text{inc}} - u_{\text{ref}}^{\text{sca}} ), \quad (2.4)$$

or the Neumann boundary condition

$$\partial_\nu u^{\text{sca}} = g( := -\partial_\nu u^{\text{inc}} - \partial_\nu u_{\text{ref}}^{\text{sca}} ). \quad (2.5)$$

Here  $\nu$  is the unit outward normal and  $\partial_\nu := \nu \cdot \nabla$  denotes the normal derivative. In addition,  $u_{\text{ref}}^{\text{sca}} = 0$  for incidence of point source. For the case of plane-wave incidence,  $u_{\text{ref}}^{\text{sca}}$  represents the reflected field resulting from the scattering of the plane wave  $u^{\text{inc}}$  by the flat surface  $\Pi$ . In particular, it is easy to deduce that

$$u_{\text{ref}}^{\text{sca}}(x) := \begin{cases} -\exp(ikx' \cdot d^{\text{inc}}), & \text{Dirichlet case,} \\ \exp(ikx' \cdot d^{\text{inc}}), & \text{Neumann case,} \end{cases}$$

where  $x' = (x_1, \dots, -x_d)$  denotes the imaging point of  $x$  w.r.t. the flat surface  $\Pi$ .

At infinity, the scattered field satisfies the following half-space Sommerfeld radiation condition:

$$\lim_{r \rightarrow \infty} r^{(n-1)/2} (\partial_r - ik) u^{\text{sca}} = 0, \quad (2.6)$$

uniformly holds in all directions for  $x_3 \geq 0$ , where  $r = |x|$ ; see the angular spectrum representation [22] and also the equivalent upward propagating radiation condition [2, 16]. For theories on direct and inverse rough-surface scattering problems, we refer readers to [3, 4, 40, 43] for more details.

## 2.2 Boundary integral equations

It follows from [22] that the scattered field  $u^{\text{sca}}$  admits the representation

$$u^{\text{sca}}(x) = \int_{\Gamma} \{G(x, y) \partial_{\nu_y} u^{\text{sca}}(y) - \partial_{\nu_y} G(x, y) u^{\text{sca}}(y)\} ds_y, \quad x \in \Omega. \quad (2.7)$$

Letting  $x \rightarrow \Gamma$  and applying the well-known jump conditions [21] lead to the BIEs on  $\Gamma$

$$\left(\frac{1}{2}I + K\right)(u^{\text{sca}})(x) = S(\partial_{\nu} u^{\text{sca}})(x), \quad x \in \Gamma, \quad (2.8)$$

$$\left(-\frac{1}{2}I + K'\right)(\partial_{\nu} u^{\text{sca}})(x) = N(u^{\text{sca}})(x), \quad x \in \Gamma, \quad (2.9)$$

wherein

$$S(\varphi)(x) := \int_{\Gamma} G(x, y) \varphi(y) ds_y, \quad x \in \Gamma, \quad (2.10)$$

$$K(\varphi)(x) := \int_{\Gamma} \partial_{\nu_y} G(x, y) \varphi(y) ds_y, \quad x \in \Gamma, \quad (2.11)$$

$$K'(\varphi)(x) := \int_{\Gamma} \partial_{\nu_x} G(x, y) \varphi(y) ds_y, \quad x \in \Gamma, \quad (2.12)$$

$$N(\varphi)(x) := \int_{\Gamma} \partial_{\nu_x} \partial_{\nu_y} G(x, y) \varphi(y) ds_y, \quad x \in \Gamma, \quad (2.13)$$

denote, respectively, the single-layer, double-layer, transpose of double-layer, and hyper-singular BIEs. Especially, the hyper-singular operator  $N$  is defined in the sense of Hadamard finite part [24].

In light of the advantages of using second-kind Fredholm integral equations for solving large-scale problems, (2.8) and (2.9) can be utilized for solving the Neumann and Dirichlet problems, respectively. However, the BIEs (2.10)-(2.13) are defined on the whole unbounded surface  $\Gamma$ , so that we require appropriate truncation strategy for the numerical implementation.

A direct truncation of the infinite boundary  $\Gamma$  in the BIEs (2.8)-(2.9) will lead to a large truncation error. In particular, a smooth windowing function is introduced in [11] for the truncation. As illustrated in that work, for plane-wave incidence, the direct windowing approach requires, for a given accuracy, increasingly large truncated domains as grazing incidence is approached. To overcome this poor performance, corrected formulations are proposed to uniform accuracy for all incident angles. However, for the case of point source, the incident field should be expressed by a superposition of plane incident waves, which means that a number of problems of plane incidence should be considered, and it is necessary to apply the Cauchy's theorem to deform the integration contour.

In [30], a PML-based BIE method is proposed for solving the two-dimensional wave scattering problems in a layered medium. This method truncates the considered infinite domain using the PML by directly imposing zero Dirichlet boundary condition on the PML boundary. Alpert's hybrid Gauss-trapezoidal quadrature rule [1] is utilized for the numerical discretization of the two-dimensional single- and double-layer BIEs and high accuracy can be achieved for incidences of plane waves and point sources. Unfortunately, quadrature rules for surface integrals that are analogous to Alpert's are still absent so far. To tackle this difficulty, we develop a high-accuracy Chebyshev-based rectangular-polar integral solver that is applicable for both line and surface integrals respectively corresponding to the two- and three-dimensional problems, for the discretization of the PML-transformed versions of all four BIEs (2.10)-(2.13) in the following.

## 3 The truncated PML problems and boundary integral equations

In this section, we briefly discuss the PML truncation strategy and introduce the reduced boundary integral equations for the truncated PML problems. The core idea of the PML is to construct artificial

layers (of finite thickness) surrounding the physical bounded domain such that the outgoing waves  $u^{\text{sca}}$  and  $\partial_\nu u^{\text{sca}}$  decay rapidly in the PML region before reaching the PML outer boundary. Then the BIEs for the truncated PML problems can be derived.

### 3.1 The PML stretching

The PML method involves analytical stretching of the real spatial coordinates of the physical equations into the complex plane, along which the outward propagating waves must be attenuated in the absorbing layer. Following the coordinate stretching approach [19], we introduce a complex change of spatial variable:  $x \in \Omega \subset \mathbb{R}^d \mapsto \tilde{x} \in \tilde{\Omega} \subset \mathbb{C}^d$  defined as

$$\tilde{x}_i(x_i) = x_i + i \int_0^{x_i} \sigma_i(t) dt \quad (3.1)$$

for  $i = 1, \dots, d$ , where we take  $\sigma_i$

$$\sigma_i(t) = \sigma_i(-t), \quad \sigma_i(t) = 0 \text{ for } |t| \leq a_i, \quad \sigma_i(t) > 0 \text{ for } |t| > a_i, \quad (3.2)$$

with  $a_i > 0, i = 1, \dots, d$ . The domains with nonzero  $\sigma_i$  are called the PML. For definiteness, throughout this paper we utilize the positive function  $\sigma_i$  [21, 29, 30]

$$\sigma_i(x_i) = \begin{cases} \frac{2Sf_1^P}{f_1^P + f_2^P}, & a_i \leq x_i \leq a_i + T_i, \\ S, & x_i > a_i + T_i, \\ 0, & -a_i < x_i < a_i, \\ \sigma_i(-x_i), & x_i \leq -a_i, \end{cases} \quad (3.3)$$

where  $T_i > 0, i = 1, \dots, d$  denote the thickness of the PML,  $P$  is a positive integer,

$$f_i = \left( \frac{1}{2} - \frac{1}{P} \right) \bar{x}_i^3 + \frac{\bar{x}_i}{P} + \frac{1}{2}, \quad f_2 = 1 - f_1, \quad \bar{x}_i = \frac{x_i - (a_i + T_i)}{T_i}.$$

It can be seen that  $\sigma_i$  maps  $[a_i, a_i + T_i]$  onto  $[0, S]$  and its derivatives vanish at  $x_i = \pm a_i$  up to order  $P-1$ . In addition, we choose  $a_i > 0$  such that the bounded Cartesian domain  $B_a := (-a_1, a_1) \times \dots \times (-a_d, a_d) \subset \mathbb{R}^d$  encloses the bounded obstacle  $U_0$  and the local defects on  $\Gamma$ . Then the infinite domain  $\Omega$  can be truncated onto a bounded domain  $\Omega^b$ , which also leads to the corresponding truncated interface  $\Gamma^b$  of  $\Gamma$ , using the box  $B_{a,T} = (-a_1 - T_1, a_1 + T_1) \times \dots \times (-a_d - T_d, a_d + T_d)$ , i.e.,  $\Omega^b = \Omega \cap B_{a,T}$  and  $\Gamma^b = \Gamma \cap B_{a,T}$ . In addition, we denote  $\Gamma^+ = \partial\Omega^b \setminus \Gamma^b$ .

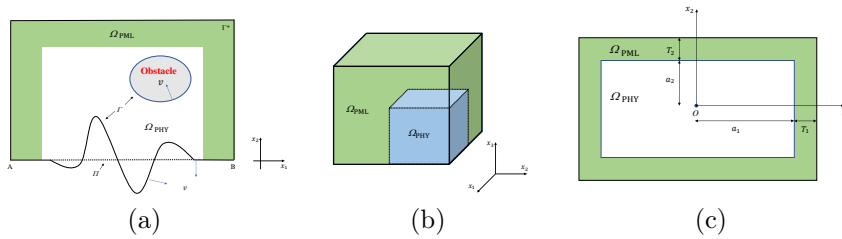


Figure 2: The PML-truncated domain  $\Omega^b$ , the physical bounded domain  $\Omega_{\text{PHY}} = B_a \cap \Omega$  and the PML region  $\Omega_{\text{PML}} = B_{a,T} \setminus \bar{B}_a$ : (a) the PML truncation in two dimensions; (b) the quarter model of PML truncation in three dimensions; (c) the vertical view of PML truncation on the bottom infinite surface in three dimensions.

### 3.2 The truncated PML problems

Relying on the complex coordinate map (3.1), the Helmholtz equation (2.3) on  $\Omega^b$  can be transformed into the following form

$$\tilde{\Delta}u^{\text{sca}}(\tilde{x}) + k^2u^{\text{sca}}(\tilde{x}) = 0, \quad \tilde{x} \in \tilde{\Omega}^b, \quad (3.4)$$

where  $\tilde{\Omega}^b = \{\tilde{x}(x)|x \in \Omega^b\}$  and  $\tilde{\Delta} = \sum_{i=1}^d \partial_{\tilde{x}_i}^2$ . Then from the Green's representation theorem [27], the solution of (3.4) can be represented by

$$u^{\text{sca}}(\tilde{x}) = \int_{\Gamma^b} \{G(\tilde{x}, y)\partial_{\nu_y}u^{\text{sca}}(y) - \partial_{\nu_y}G(\tilde{x}, y)u^{\text{sca}}(y)\} ds_y, \quad \tilde{x} \in \tilde{\Omega}^b. \quad (3.5)$$

Defining the complex function  $\tilde{u}^{\text{sca}}(x) = u^{\text{sca}}(\tilde{x})$  in  $\Omega^b$ , we can rewrite the equation (3.4) as

$$\nabla \cdot (\mathbf{A}\nabla\tilde{u}^{\text{sca}}) + k^2J\tilde{u}^{\text{sca}} = 0, \quad x \in \Omega^b, \quad (3.6)$$

where

$$\begin{aligned} \alpha_i(x_i) &= 1 + i\sigma_i(x_i), \quad i = 1, \dots, d, \\ \mathbf{A} &= \begin{cases} \text{diag}\{\alpha_2/\alpha_1, \alpha_1/\alpha_2\}, & d = 2, \\ \text{diag}\{\alpha_2\alpha_3/\alpha_1, \alpha_1\alpha_3/\alpha_2, \alpha_1\alpha_2/\alpha_3\}, & d = 3, \end{cases} \\ J &= \begin{cases} \alpha_1\alpha_2, & d = 2, \\ \alpha_1\alpha_2\alpha_3, & d = 3. \end{cases} \end{aligned}$$

On  $\Gamma^b$ , the original Dirichlet and Neumann boundary conditions on  $\Gamma$  can be reduced to

$$\tilde{u}^{\text{sca}} = \tilde{f}(x) \quad (:= f(\tilde{x})),$$

and

$$\tilde{\partial}_\nu\tilde{u}^{\text{sca}} = \tilde{g}(x) \quad (:= g(\tilde{x})),$$

respectively, where  $\tilde{\partial}_\nu = (\mathbf{A}^\top\nu) \cdot \nabla$ . Sommerfeld's radiation condition (2.6) implies that  $u^{\text{sca}}$  is outgoing so that the complexified fields  $\tilde{u}^{\text{sca}}$  and  $\tilde{\partial}_\nu\tilde{u}^{\text{sca}}$  decay exponentially as  $|x| \rightarrow \infty$ . Thus, it is highly accurate to directly assume that  $\tilde{u}^{\text{sca}} = 0$  and  $\tilde{\partial}_\nu\tilde{u}^{\text{sca}} = 0$  on  $\Gamma^+$ .

### 3.3 Boundary integral equations

As shown in [27], the fundamental solution of (3.6), called PML-transformed free-space Green's function, takes the form

$$\tilde{G}(x, y) = G(\tilde{x}, \tilde{y}) = \begin{cases} \frac{i}{4}H_0^{(1)}(k\rho(\tilde{x}, \tilde{y})), & d = 2, \\ \frac{\exp(ik\rho(\tilde{x}, \tilde{y}))}{4\pi\rho(\tilde{x}, \tilde{y})}, & d = 3, \end{cases}$$

where  $\rho$  is the complex distance function given by

$$\rho(\tilde{x}, \tilde{y}) = \left( \sum_{j=1}^d (\tilde{x}_j - \tilde{y}_j)^2 \right)^{1/2} \quad (3.7)$$

and the half-power operator  $z^{1/2}$  is chosen to be the branch of  $\sqrt{z}$  with nonnegative real part for  $z \in \mathbb{C} \setminus (-\infty, 0]$  such that  $\arg\sqrt{z} \in (-\frac{\pi}{2}, \frac{\pi}{2}]$ .

According to [30] and noting that we have assumed that  $\tilde{u}^{\text{sca}} \approx 0$  and  $\partial_{\nu_c} \tilde{u}^{\text{sca}} \approx 0$  on  $\Gamma^+$ , the solution of (3.6) can be approximately represented in the form

$$\tilde{u}^{\text{sca}}(x) = \int_{\Gamma^b} \left\{ \tilde{G}(x, y) \tilde{\partial}_{\nu_y} \tilde{u}^{\text{sca}}(y) - \tilde{\partial}_{\nu_y} \tilde{G}(x, y) \tilde{u}^{\text{sca}}(y) \right\} ds_y, \quad x \in \Omega^b. \quad (3.8)$$

Taking the limits as  $x \rightarrow \Gamma^b$  and applying the jump conditions, we obtain the corresponding BIEs on  $\Gamma^b$

$$\left( \frac{1}{2}I + \tilde{K} \right) (\tilde{u}^{\text{sca}})(x) = \tilde{S}(\tilde{\partial}_{\nu} \tilde{u}^{\text{sca}})(x), \quad x \in \Gamma^b, \quad (3.9)$$

$$\left( -\frac{1}{2}I + \tilde{K}' \right) (\tilde{\partial}_{\nu} \tilde{u}^{\text{sca}})(x) = \tilde{N}(\tilde{u}^{\text{sca}})(x), \quad x \in \Gamma^b, \quad (3.10)$$

where the boundary integral operators  $\tilde{S}$ ,  $\tilde{K}$ ,  $\tilde{K}'$  and  $\tilde{N}$  are defined by (2.10), (2.11), (2.12) and (2.13) with  $G$  replaced by  $\tilde{G}$ ,  $\partial_{\nu}$  replaced by  $\tilde{\partial}_{\nu}$  and  $\Gamma$  replaced by  $\Gamma^b$ , respectively.

Analogous to the discussion in Section 2.2, we use the BIEs (3.9) and (3.10) to solve the corresponding Neumann and Dirichlet problems, respectively. The given Dirichlet and Neumann data on  $\Gamma$  imply the following two BIEs:

$$\left( \frac{1}{2}I + \tilde{K} \right) (\tilde{u}^{\text{sca}})(x) = \tilde{S}(\tilde{g})(x), \quad x \in \Gamma^b, \quad (3.11)$$

and

$$\left( -\frac{1}{2}I + \tilde{K}' \right) (\tilde{\partial}_{\nu} \tilde{u}^{\text{sca}})(x) = \tilde{N}(\tilde{f})(x), \quad x \in \Gamma^b. \quad (3.12)$$

## 4 Numerical implementation

This section will discuss the numerical discretization of the boundary integral operators  $\tilde{S}$ ,  $\tilde{K}$ ,  $\tilde{K}'$  and  $\tilde{N}$  by means of the Chebyshev-based rectangular-polar integral solver [9, 13]. Before that, regularized formulations will be derived in the following subsection to treat the hyper-singular operator  $\tilde{N}$ .

### 4.1 Regularization of the hyper-singular operator

As shown in the following lemma, by analogy to Maue's identity [26, 32], the hyper-singular operator  $\tilde{N}$  can be reformulated as a combination of weakly-singular integral operators and tangential derivatives.

**Lemma 4.1.** *Assuming that  $\varphi = 0$  on  $\partial\Gamma^b$ . In two dimensions, the hyper-singular operator  $\tilde{N}$  can be expressed in the form*

$$\tilde{N}(\varphi)(x) = \frac{d}{ds_x} \int_{\Gamma^b} \tilde{G}(x, y) \frac{d\varphi}{ds_y} ds_y + k^2 \int_{\Gamma^b} \nu_x^\top \mathbf{A}_1(x, y) \nu_y \tilde{G}(x, y) \varphi(y) ds_y,$$

where  $\mathbf{A}_1(x, y) = \text{diag}\{\alpha_2(x_2)\alpha_2(y_2), \alpha_1(x_1)\alpha_1(y_1)\}$  and  $\frac{d}{ds} = \nu^\perp \cdot \nabla$  denotes the tangential derivative. In three dimensions, we have

$$\begin{aligned} \tilde{N}(\varphi)(x) = & \int_{\Gamma^b} \left( \mathbf{A}_2(x, y) (\nu_x \times \nabla_x) \tilde{G}(x, y) \right) \cdot (\nu_y \times \nabla_y) \varphi(y) ds_y \\ & + k^2 \int_{\Gamma^b} \nu_x^\top \mathbf{A}_3(x, y) \nu_y \tilde{G}(x, y) \varphi(y) ds_y, \end{aligned}$$

where

$$\begin{aligned} \mathbf{A}_2(x, y) = & \text{diag}\{\alpha_1(x_1)\alpha_1(y_1), \alpha_2(x_2)\alpha_2(y_2), \alpha_3(x_3)\alpha_3(y_3)\}, \\ \mathbf{A}_3(x, y) = & \text{diag}\left\{ \frac{\alpha(x, y)}{\alpha_1(x_1)\alpha_1(y_1)}, \frac{\alpha(x, y)}{\alpha_2(x_2)\alpha_2(y_2)}, \frac{\alpha(x, y)}{\alpha_3(x_3)\alpha_3(y_3)} \right\}, \end{aligned}$$

with  $\alpha(x, y) = \prod_{i=1}^3 \alpha_i(x_i) \alpha_i(y_i)$ .

*Proof.* Here we only give the proof of three-dimensional case and the proof of two-dimensional case can be carried out analogously. The hyper-singular operator  $\tilde{N}$  is given by

$$\tilde{N}(\varphi)(x) = \tilde{\partial}_{\nu_x} \int_{\Gamma^b} \tilde{\partial}_{\nu_y} \tilde{G}(x, y) \varphi(y) ds_y, \quad x \in \Gamma^b.$$

Noting that

$$\tilde{\partial}_{\nu_y} \tilde{G}(x, y) = [\alpha_2(y_2) \alpha_3(y_3) \nu_y^1 \partial_{\tilde{y}_1} + \alpha_1(y_1) \alpha_3(y_3) \nu_y^2 \partial_{\tilde{y}_2} + \alpha_1(y_1) \alpha_2(y_2) \nu_y^3 \partial_{\tilde{y}_3}] \tilde{G}(x, y),$$

and

$$\nabla \cdot (\mathbf{A} \nabla \tilde{G}(x, y)) + k^2 J \tilde{G}(x, y) = 0, \quad x \neq y,$$

it can be derived that

$$\begin{aligned} & \mathbf{A} \nabla_x \tilde{\partial}_{\nu_y} \tilde{G}(x, y) \\ &= \mathbf{C}(x, y) (\nu_y \times \nabla_y) \tilde{G}(x, y) + k^2 \begin{bmatrix} \alpha_2(x_2) \alpha_2(y_2) \alpha_3(x_3) \alpha_3(y_3) \nu_y^1 \\ \alpha_1(x_1) \alpha_1(y_1) \alpha_3(x_3) \alpha_3(y_3) \nu_y^2 \\ \alpha_1(x_1) \alpha_1(y_1) \alpha_2(x_2) \alpha_2(y_2) \nu_y^3 \end{bmatrix} \tilde{G}(x, y). \end{aligned}$$

where

$$\mathbf{C}(x, y) = \begin{bmatrix} 0 & \alpha_2(x_2) \alpha_3(x_3) \alpha_2(y_2) \partial_{\tilde{x}_3} & -\alpha_2(x_2) \alpha_3(x_3) \alpha_3(y_3) \partial_{\tilde{x}_2} \\ -\alpha_1(x_1) \alpha_3(x_3) \alpha_1(y_1) \partial_{\tilde{x}_3} & 0 & \alpha_1(x_1) \alpha_3(x_3) \alpha_3(y_3) \partial_{\tilde{x}_1} \\ \alpha_1(x_1) \alpha_2(x_2) \alpha_1(y_1) \partial_{\tilde{x}_2} & -\alpha_1(x_1) \alpha_2(x_2) \alpha_2(y_2) \partial_{\tilde{x}_1} & 0 \end{bmatrix}.$$

Then the Stokes formula yields

$$\begin{aligned} N(\varphi)(x) &= \int_{\Gamma^b} \begin{bmatrix} \alpha_1(x_1) \alpha_1(y_1) (\nu_x^2 \partial_{x_3} - \nu_x^3 \partial_{x_2}) \\ \alpha_2(x_2) \alpha_2(y_2) (\nu_x^3 \partial_{x_1} - \nu_x^1 \partial_{x_3}) \\ \alpha_3(x_3) \alpha_3(y_3) (\nu_x^1 \partial_{x_2} - \nu_x^2 \partial_{x_1}) \end{bmatrix}^\top \tilde{G}(x, y) (\nu_y \times \nabla_y) \varphi(y) ds_y \\ &+ k^2 \int_{\Gamma^b} \nu_x^\top \begin{bmatrix} \alpha_2(x_2) \alpha_2(y_2) \alpha_3(x_3) \alpha_3(y_3) \nu_y^1 \\ \alpha_1(x_1) \alpha_1(y_1) \alpha_3(x_3) \alpha_3(y_3) \nu_y^2 \\ \alpha_1(x_1) \alpha_1(y_1) \alpha_2(x_2) \alpha_2(y_2) \nu_y^3 \end{bmatrix} \tilde{G}(x, y) \varphi(y) ds_y \\ &= \int_{\Gamma^b} (\mathbf{A}_2(x, y) (\nu_x \times \nabla_x) \tilde{G}(x, y)) \cdot (\nu_y \times \nabla_y) \varphi(y) ds_y \\ &+ k^2 \int_{\Gamma^b} \nu_x^\top \mathbf{A}_3(x, y) \nu_y \tilde{G}(x, y) \varphi(y) ds_y, \end{aligned}$$

and this completes the proof.  $\square$

**Remark 4.2.** For the numerical discretization of (3.12), it requires to treat the term  $\tilde{N}(\tilde{f})$ .

- For the case of a plane incident wave, it is known that  $f = 0$  on  $\Pi$  and thus,  $\tilde{f} = 0$  on  $\partial\Gamma^b$ . Hence, the regularized formulations shown in Lemma 4.1 holds exactly.
- For the case of a point source,  $f = -G(x, z)$  for  $x \in \Gamma$ . Noting that  $G(x, z)$  is an outgoing wave, the complex coordinate transform indicates that  $G(\tilde{x}, z)$  decays exponentially as  $|x| \rightarrow \infty$ . Thus, we have  $\tilde{f} \approx 0$  on  $\partial\Gamma^b$ . Then the regularized formulations shown in Lemma 4.1 can be viewed as an approximation of  $\tilde{N}(\tilde{f})$ .



## 4.2 Chebyshev-based rectangular-polar solver

Relying on the regularization of the hyper-singular operator proposed in the previous subsection, the discretizations of the BIOs  $\tilde{S}$ ,  $\tilde{K}$ ,  $\tilde{K}'$  and  $\tilde{N}$  can be degenerated into the discretization of

(i) the integral operators of the form

$$\mathcal{H}(\varphi)(x) = \int_{\Gamma^b} H(x, y)\varphi(y)ds_y, \quad x \in \Gamma^b, \quad (4.1)$$

in which the kernel  $H(x, y)$  is piece-wise weakly-singular;

(ii) the tangential derivative operators  $\frac{d}{ds}$  and  $\nu \times \nabla$ .

In this work, the Chebyshev-based rectangular-polar solver and the Chebyshev-based differentiation algorithm proposed in [9, 13] will be applied for numerical evaluations of (i) and (ii), respectively. For simplicity, we only give a brief description for the three-dimensional case. For the two-dimensional case, we refer to [14].

Let the surface  $\Gamma^b$  be partitioned into a set of non-overlapping parameterized patches  $\Gamma_q$ ,  $q = 1, \dots, M$  as

$$\Gamma^b = \bigcup_{q=1}^M \Gamma_q, \quad \Gamma_q = \left\{ x = \mathbf{r}^q(u, v) : [-1, 1]^2 \rightarrow \mathbb{R}^3 \right\}.$$

Then the integrals  $\mathcal{H}\varphi(x)$  over  $\Gamma^b$  can be split into the sum of integrals over each of the  $M$  patches,

$$\mathcal{H}(\varphi)(x) = \sum_{q=1}^M \mathcal{H}_q(x), \quad \mathcal{H}_q(x) := \int_{\Gamma_q} H(x, y)\varphi(y)ds_y, \quad x \in \Gamma^b.$$

Denoting by  $u_j, v_j \in [-1, 1]$  ( $j = 0, \dots, N-1$ ) the  $N$  Chebyshev points

$$u_j = \cos\left(\frac{2j+1}{2N}\pi\right), \quad v_j = \cos\left(\frac{2j+1}{2N}\pi\right), \quad j = 0, \dots, N-1,$$

we can define the discretization points on each  $\Gamma_q$  by

$$x_{ij}^q = \mathbf{r}^q(u_i, v_j), \quad i, j = 0, \dots, N-1.$$

Given a density  $\varphi$ , it can then be approximated on  $\Gamma_q$  by the Chebyshev polynomials as

$$\varphi(x) \approx \sum_{i,j=0}^{N-1} \varphi_{ij}^q a_{ij}(u, v) = \sum_{i,j=0}^{N-1} \varphi(x_{ij}^q) a_{ij}(u, v), \quad x \in \Gamma_q,$$

where

$$a_{ij}(u, v) = \frac{1}{N^2} \sum_{m,n=0}^{N-1} \alpha_n \alpha_m T_n(u_i) T_m(v_j) T_n(u) T_m(v), \quad \alpha_n = \begin{cases} 1, & n = 0, \\ 2, & n \neq 0. \end{cases}$$

The strategy for evaluating the integral  $\mathcal{H}_q(x)$  depends on the distance between the point  $x$  and the  $q$ -th patch  $\Gamma_q$ . Define the distance

$$\text{dist}_{x, \Gamma_q} := \min_{(u,v) \in [-1,1]^2} \{|x - \mathbf{r}^q(u, v)|\}$$

and the value

$$(\tilde{u}^q, \tilde{v}^q) = \underset{(u,v) \in [-1,1]^2}{\text{argmin}} \{|x - \mathbf{r}^q(u, v)|\}.$$

Let  $\delta > 0$  be a given tolerance, where in our settings,  $\delta = 0.1$ . If  $\text{dist}_{x, \Gamma_q} > \delta$ , called "non-adjacent" integration case, the integral is smooth, which can be accurately by means of Fejér's first quadrature rule. For the "adjacent" integration case (i.e.,  $\text{dist}_{x, \Gamma_q} \leq \delta$ ), the integrals  $\mathcal{H}_q(x)$  will be nearly/completely singular. In order to tackle this difficulty, we construct a new graded mesh, by means of appropriate "rectangular-polar" changes of variables

$$\xi_\alpha(t) = \begin{cases} \text{sgn}(t) - (\text{sgn}(t) - \alpha)\chi_p(1 - |t|), & \alpha \neq \pm 1, \\ -1 + 2\chi_p\left(\frac{|t+1|}{2}\right), & \alpha = 1, \\ 1 - 2\chi_p\left(\frac{|t-1|}{2}\right), & \alpha = -1, \end{cases} \quad t \in [-1, 1],$$

where  $-1 \leq \alpha \leq 1$ , and for a given integer  $p$ ,  $\chi_p$  is given by

$$\chi_p(s) = 2 \frac{[\eta_p(s)]^p}{[\eta_p(s)]^p + [\eta_p(-s)]^p} - 1, \quad -1 \leq s \leq 1,$$

with

$$\eta_p(s) = \left(\frac{1}{2} - \frac{1}{p}\right)s^3 + \frac{1}{p}s + \frac{1}{2}.$$

The changes of variables, with both  $\alpha = \tilde{u}^q$  and  $\alpha = \tilde{v}^q$  can be used to produce a refinement around the points  $\tilde{u}^q$  and  $\tilde{v}^q$ . Then applying the Chebyshev expansion of  $\varphi$ , we have

$$\mathcal{H}_q(x) \approx \sum_{m,n=0}^{N-1} A_{nm}^q \varphi_{nm}^q,$$

where

$$A_{nm}^q = \sum_{l_1, l_2=0}^{N_\beta-1} H(x, \mathbf{r}^q(\xi_{\tilde{u}^q}(\tilde{t}_{l_1}), \xi_{\tilde{v}^q}(\tilde{t}_{l_2}))) J^q(\xi_{\tilde{u}^q}(\tilde{t}_{l_1}), \xi_{\tilde{v}^q}(\tilde{t}_{l_2})) \\ \times a_{nm}(\xi_{\tilde{u}^q}(\tilde{t}_{l_1}), \xi_{\tilde{v}^q}(\tilde{t}_{l_2})) \xi'_{\tilde{u}^q}(\tilde{t}_{l_1}) \xi'_{\tilde{v}^q}(\tilde{t}_{l_2}) \tilde{w}_{l_1} \tilde{w}_{l_2},$$

with the quadrature nodes and weights given by

$$\tilde{t}_j = \cos\left(\frac{2j+1}{2N_\beta}\pi\right), \quad j = 0, \dots, N_\beta - 1,$$

and

$$\tilde{w}_j = \frac{2}{N_\beta} \left(1 - 2 \sum_{l=1}^{\lfloor N_\beta/2 \rfloor} \frac{1}{4l^2 - 1} \cos(l\tilde{t}_j)\right), \quad j = 0, \dots, N_\beta - 1.$$

Finally, we describe the approximations of the tangential derivative operator  $\frac{d}{ds}$  and  $\nu \times \nabla$ . Note that  $\nu \times \nabla = \nu \times \nabla^S$  where  $\nabla^S$  denotes the surface gradient. On each patch  $\Gamma_q$ , the quantities  $\frac{d\varphi}{ds}$  and  $\nabla^S \varphi$  can be easily evaluated by means of term-by-term differentiation of the Chebyshev expansion of  $\varphi$ . In two dimensions, we can obtain that

$$\frac{d\varphi}{ds}(\mathbf{r}^q(u)) = \sum_{i=0}^{N-1} \left| \frac{d\mathbf{r}^q(u)}{du} \right|^{-1} \frac{da_i(u)}{du} \varphi_i^q.$$

In three dimensions, the evaluation of the tangential-derivative operator  $\nu \times \nabla^S$  can be achieved by using the expressions of  $\nabla^S$  on parameterized curve, see [13, Section 4.2.2].

**Remark 4.3.** *If corners or edges exist on  $\Gamma^b$ , then the unknowns in the integral equations have singularities at the corners or edges. To resolve the singularities, we utilize a change of variables whose derivatives vanish at corners or along edges. A change of variables can be devised on the basis of mappings  $\chi_p(s)$ , whose derivatives up to order  $p - 1$  vanish at the endpoints. Then the function  $\chi_p(s)$  can be used to construct a change of variables to accurately resolve field singularities at the corners or edges (for more details, see [9, 21]).*

### 4.3 Layered-medium scattering problems

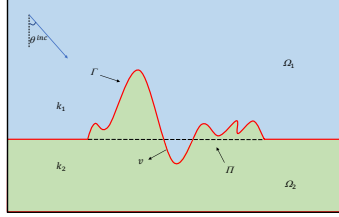


Figure 3: Description of the problem under consideration: scattering by a defect on a penetrable layer.  $\Gamma$  denotes the interface between the two media, and  $\Phi$  denotes the interface between the upper and lower half-planes.

To conclude this section, we briefly discuss how to the new PML-based BIE solver be extended to layered-medium scattering problems. Without loss of generality, we focus on the acoustic scattering problems in a two-layer medium in two dimensions, see Fig. 3. The method proposed in [30] uses the Neumann-to-Dirichlet map to construct the boundary integral equations. Alternatively, in this work, we utilize the second-kind system of integral equations derived in [25] which covers all four BIOs (2.10)-(2.13).

Analogous to Section 2.1, let  $u^{\text{inc}}$  be a plane incident wave in  $\Omega^1$  given in (2.1) and  $u_{j,\text{ref}}^{\text{sca}}$  be the reference scattered fields in  $\Omega_j, j = 1, 2$ , resulting from the scattering of the plane wave  $u^{\text{inc}}$  by the flat surface  $\Pi$ ; see [30] for more details. Then, the acoustic scattering problems can be formulated as follows: the scattered fields  $u_j^{\text{sca}}, j = 1, 2$  satisfy the Helmholtz equation

$$\Delta u_j^{\text{sca}} + k_j^2 u_j^{\text{sca}} = 0 \quad \text{in } \Omega_j, \quad j = 1, 2,$$

where  $k_j$  is the wavenumber in  $\Omega_j$ , and the transmission conditions on  $\Gamma$  are

$$\begin{aligned} u_1^{\text{sca}}|_{\Gamma} - u_2^{\text{sca}}|_{\Gamma} &= f (:= -u^{\text{inc}}|_{\Gamma} - u_{1,\text{ref}}^{\text{sca}}|_{\Gamma} + u_{2,\text{ref}}^{\text{sca}}|_{\Gamma}), \\ \partial_{\nu} u_1^{\text{sca}}|_{\Gamma} - \partial_{\nu} u_2^{\text{sca}}|_{\Gamma} &= g (:= -\partial_{\nu} u^{\text{inc}}|_{\Gamma} - \partial_{\nu} u_{1,\text{ref}}^{\text{sca}}|_{\Gamma} + \partial_{\nu} u_{2,\text{ref}}^{\text{sca}}|_{\Gamma}). \end{aligned}$$

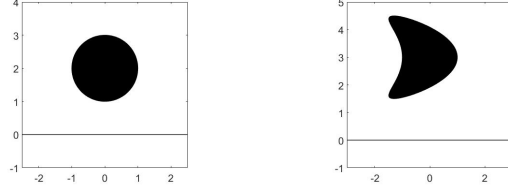
They lead to the following integral equation system

$$\begin{bmatrix} I + K_1 - K_2 & S_2 - S_1 \\ N_1 - N_2 & I + K'_2 - K'_1 \end{bmatrix} \begin{bmatrix} u_2^{\text{sca}}|_{\Gamma} \\ \partial_{\nu} u_2^{\text{sca}}|_{\Gamma} \end{bmatrix} = \begin{bmatrix} -f \\ -g \end{bmatrix},$$

where the subscripts 1 and 2 in the BIOs indicate that they are defined for the wave numbers  $k_1$  and  $k_2$ , respectively. Applying the PML stretching and assuming that the corresponding solutions  $\tilde{u}_j^{\text{sca}}, j = 1, 2$  to the PML truncated problems vanish on the outer boundary of PML region, we can obtain the reduced BIEs:

$$\begin{bmatrix} I + \tilde{K}_1 - \tilde{K}_2 & \tilde{S}_2 - \tilde{S}_1 \\ \tilde{N}_1 - \tilde{N}_2 & I + \tilde{K}'_2 - \tilde{K}'_1 \end{bmatrix} \begin{bmatrix} \tilde{u}_2^{\text{sca}}|_{\Gamma} \\ \partial_{\nu} \tilde{u}_2^{\text{sca}}|_{\Gamma} \end{bmatrix} = \begin{bmatrix} -\tilde{f} \\ -\tilde{g} \end{bmatrix}.$$

Numerical schemes in the previous two subsections can be used to directly discretize the integral operators so as to obtain  $\tilde{u}_2^{\text{sca}}|_{\Gamma}$  and  $\partial_{\nu} \tilde{u}_2^{\text{sca}}|_{\Gamma}$  numerically.



(a) disc within half-space (b) kite within half-space

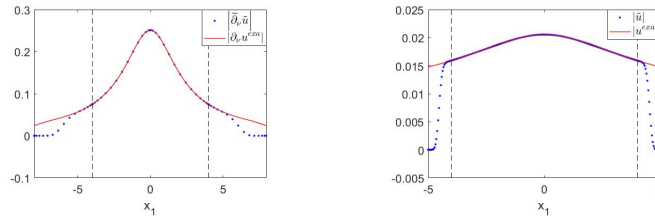
Figure 4: Two half-space in two dimensions considered in this paper.

## 5 Numerical experiments

In this section, we present a variety of numerical results to demonstrate the accuracy and efficiency of the proposed PML-based BIE methods for solving two- and three-dimensional acoustic half-space problems. Solutions of the various integral equations were produced by means of the fully complex version of the iterative solver GMRES with residual tolerance  $\epsilon_r$  as specified in each case and the relative maximum error is defined by

$$\epsilon_\infty := \frac{\max_{x \in \Gamma_{\text{test}}} |u^{\text{num}}(x) - u^{\text{ref}}(x)|}{\max_{x \in \Gamma_{\text{test}}} |u^{\text{ref}}(x)|}, \quad (5.1)$$

where  $u^{\text{ref}}$  is produced through evaluation of exact solutions, when available, or by means of numerical solution with sufficiently fine discretizations, and where  $\Gamma_{\text{test}}$  is a suitably selected line segment (2D) or square plane (3D) above the defect. In all cases, we choose  $N^\beta = 200$ ,  $P = 6$ ,  $S = 6$  and the PML thickness  $T_i$  is set to be  $T_i = 2\lambda = 2 \times \frac{2\pi}{k}$ ,  $i = 1, \dots, d$ , where  $\lambda$  denotes the free-space wavelength. All of the numerical results presented in this paper were obtained by means of Fortran implementations, parallelized using OpenMP.



(a) Dirichlet problem ( $k = \pi$ ) (b) Neumann problem ( $k = 10\pi$ )

Figure 5: (a) Absolute values of  $\tilde{\partial}_\nu \tilde{u}^{\text{sca}}$  and  $\partial_\nu u^{\text{exa}}$  on  $\partial\Omega^b \cap \Pi$  for Dirichlet problem with  $k = \pi$ ; (b) Absolute values of  $\tilde{u}^{\text{sca}}$  and  $u^{\text{exa}}$  on  $\partial\Omega^b \cap \Pi$  with  $k = 10\pi$ ; dashed lines separate  $\partial\Omega_{\text{PML}} \cap \Pi$  and  $\partial\Omega_{\text{PHY}} \cap \Pi$ .

### 5.1 Two-dimensional examples

In this subsection, we will test the accuracy and efficiency of the PML-based BIE methods for the two-dimensional problems with geometrical settings shown in Fig. 4 wherein the thin black lines denote the impenetrable infinite boundary. To test the accuracy of the proposed solver, we consider the exact solution  $u^{\text{exa}}(x, z) = G(x, z)$  with  $z = (0, 2)$  for Fig. 4(a) and  $z = (0, 3)$  for Fig. 4(b), respectively, and the corresponding boundary data is given by  $f = u^{\text{exa}}(x, z)$  and  $g = \partial_\nu u^{\text{exa}}(x, z)$ . We set  $a_1 = 4$ .

Firstly, we consider the Dirichlet problem of Fig. 4(a) with  $k = \pi$  and the Neumann problem of Fig. 4(b) with  $k = 10\pi$ . Fig. 5 presents the absolute values of the numerical solutions of BIEs (3.11)-(3.12) on  $\Gamma^b$ . It shows that the numerical solutions match perfectly with the exact data on  $\partial\Omega_{\text{PHY}} \cap \Pi$ , and

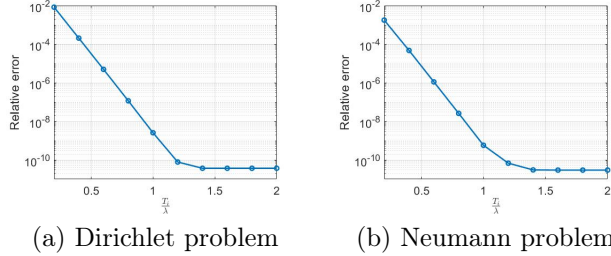


Figure 6: Numerical errors  $\epsilon_\infty$  with respect to  $\frac{T_l}{\lambda}$

Table 1: Numerical errors  $\epsilon_\infty$  for the Dirichlet and Neumann problems of scattering by a disc-shaped obstacle within a half-space.

$k$	$N$	$N_{\text{DOF}}$	Dirichlet problem		Neumann problem	
			$N_{\text{iter}}$	$\epsilon_\infty$	$N_{\text{iter}}$	$\epsilon_\infty$
$\pi$	16	$6 \times 16$	16	$3.92 \times 10^{-3}$	12	$5.42 \times 10^{-5}$
	32	$6 \times 32$	13	$1.61 \times 10^{-6}$	12	$2.66 \times 10^{-8}$
	64	$6 \times 64$	13	$2.29 \times 10^{-11}$	12	$7.64 \times 10^{-13}$
$10\pi$	32	$12 \times 32$	48	$5.81 \times 10^{-3}$	46	$2.17 \times 10^{-4}$
	48	$12 \times 48$	47	$5.10 \times 10^{-4}$	44	$1.63 \times 10^{-5}$
	64	$12 \times 64$	46	$4.69 \times 10^{-8}$	45	$1.93 \times 10^{-9}$

decay rapidly when approaching the endpoints of  $\Gamma^b$ . Next, we choose  $k = 2\pi$  and compute relative errors for different values of  $\frac{T_l}{\lambda}$ , as shown in Fig. 6. We can observe that the relative errors decay exponentially with the increase of PML thickness before the discretization error dominates the total error. It can also be seen that one can get sufficiently accurate solutions by choosing PMLs with a thickness of twice wavelength. Tables 1 and 2 display the numerical errors  $\epsilon_\infty$  for different degrees of freedom  $N_{\text{DOF}}$  as well as the corresponding numbers of iterations required by GMRES to achieve the residual tolerance  $\epsilon_r = 10^{-12}$ . This clearly demonstrates the high accuracy of the proposed PML-based BIE solver. Next, we consider the scattering of the plane incident wave (2.1) with  $\theta^{\text{inc}} = \frac{\pi}{4}$  and point source (2.2) located at  $z = (2, 5) \in \Omega$ . Figs. 7 and 8 show the distribution of the total fields resulting from the PML-based BIE method for these two cases, respectively.

## 5.2 Three-dimensional examples

In this subsection, we demonstrate the performance of the proposed method for solving the three-dimensional scattering problems and the considered bounded obstacles on the half-space  $\mathbb{R}_+^3$  are depicted in Fig. 9. Analogous to the discussion in two dimensions, we let  $u^{\text{exa}}(x, z) = G(x, z)$  be the exact solution,

Table 2: Numerical errors  $\epsilon_\infty$  for the Dirichlet and Neumann problems of scattering by a kite-shaped obstacle within a half-space.

$k$	$N$	$N_{\text{DOF}}$	Dirichlet problem		Neumann problem	
			$N_{\text{iter}}$	$\epsilon_\infty$	$N_{\text{iter}}$	$\epsilon_\infty$
$\pi$	16	$10 \times 16$	22	$3.84 \times 10^{-3}$	21	$6.65 \times 10^{-4}$
	32	$10 \times 32$	22	$1.53 \times 10^{-6}$	21	$2.09 \times 10^{-7}$
	64	$10 \times 64$	22	$1.00 \times 10^{-10}$	21	$3.90 \times 10^{-11}$
$10\pi$	32	$15 \times 32$	108	$1.69 \times 10^{-2}$	104	$1.30 \times 10^{-3}$
	48	$15 \times 48$	108	$1.52 \times 10^{-4}$	104	$2.58 \times 10^{-5}$
	64	$15 \times 64$	108	$5.49 \times 10^{-8}$	104	$3.31 \times 10^{-9}$

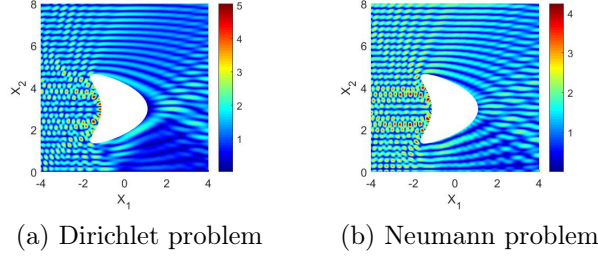


Figure 7: Absolute values of the total field for the Dirichlet and Neumann problems of scattering of a plane pressure wave by a kite-shaped obstacle, where  $k = 5\pi$ .

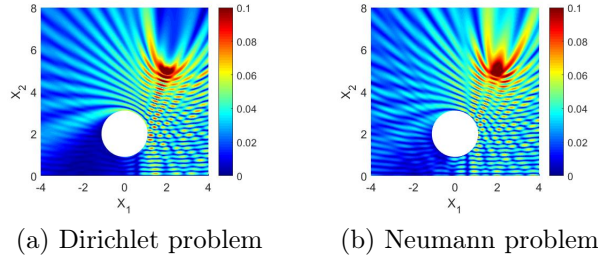


Figure 8: Absolute values of the total field for the Dirichlet and Neumann problems of scattering of an incident point source by a disc-shaped obstacle, where  $k = 5\pi$ .

where  $z = (0, 0, 2)$  locates inside the obstacles. We always set  $a_1 = a_2 = 2$ .

In our first example, we consider the problems of Fig. 9 (a) with  $k = \pi$  and Fig. 9 (b) with  $k = 10\pi$ , and Fig. 10 and 11 display the absolute values of the numerical solutions of BIEs (3.11)-(3.12) on  $\Gamma^b$ , respectively. Here, 42 patches are selected for the boundary partitioning. It can be seen that the numerical solutions match perfectly with the exact data on  $\partial\Omega_{\text{PHY}} \cap \Pi$ , and decay rapidly on PML interface  $\partial\Omega_{\text{PML}} \cap \Pi$ . Choosing  $k = 2\pi$ , the relative errors for different values of  $\frac{T_i}{\lambda}$  are depicted in Fig. 12, which show that the relative errors decay exponentially with the increase of PML thickness and setting the PML thickness to twice the wavelength can obtain sufficiently accurate solutions. Fig. 13 presents the relative errors  $\epsilon_\infty$  with respect to different  $N$  (number of Chebyshev points in each patch) for the Dirichlet and Neumann problems with  $k = \pi$ , which clearly demonstrates the efficiency the proposed PML-based BIE solver for three-dimensional problems. Higher accuracy can be achieved by increasing the number  $N^\beta$  and evaluating the integral kernels more carefully. Table 3 lists the numerical errors together with other statistics such as pre-computation time, time per iteration and number of iterations used for the scattering problems at frequencies  $k = \pi$ ,  $k = 4\pi$  and  $k = 10\pi$ .

Next, we consider the scattering of the plane incident wave (2.1) with angle pair  $\theta^{\text{inc}} = \frac{\pi}{3}$ ,  $\phi^{\text{inc}} = 0$  and point source (2.2) located at  $z = (0, 3, 3) \in \Omega$ . Fig. 14 and 15 show the distribution of the total fields with  $k = 4\pi$  resulting from the PML-based BIE method.

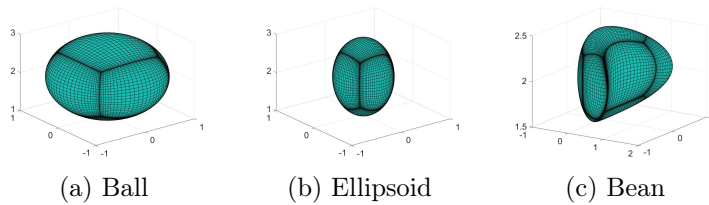


Figure 9: Obstacles used in the numerical tests presented in Section 5.2.

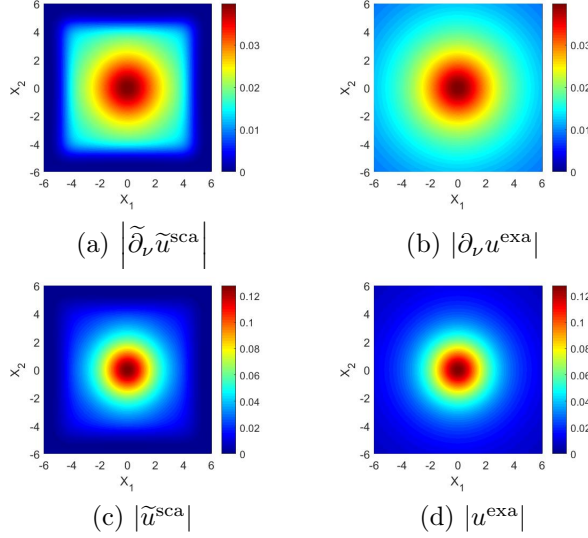


Figure 10: (a)(b): Absolute values of the  $\partial_\nu \tilde{u}^{\text{sca}}$  and  $\partial_\nu u^{\text{exa}}$  for the Dirichlet problem; (c)(d): Absolute values of the  $\tilde{u}^{\text{sca}}$  and  $u^{\text{exa}}$  for the Neumann problem. Here,  $k = \pi$ .

Table 3: Numerical errors and computing costs for the Dirichlet and Neumann problems of scattering by the obstacle Fig. 9(a) on the half-space.

$\omega$	$N_{DOF}$	Dirichlet problem			
		Time(prec.)	Time(1 iter.)	$N_{iter}(\epsilon_r)$	$\epsilon_\infty$
$\pi$	43008	2.02 min	8.23 s	10( $3.57 \times 10^{-10}$ )	$5.54 \times 10^{-7}$
$4\pi$	43008	1.17 min	5.14 s	21( $2.76 \times 10^{-8}$ )	$3.54 \times 10^{-6}$
$10\pi$	96768	5.11 min	34.26 s	40 ( $5.73 \times 10^{-6}$ )	$1.45 \times 10^{-5}$
$\omega$	$N_{DOF}$	Neumann problem			
		Time(prec.)	Time(1 iter.)	$N_{iter}(\epsilon_r)$	$\epsilon_\infty$
$\pi$	43008	1.65 min	7.57 s	9( $9.45 \times 10^{-10}$ )	$6.19 \times 10^{-8}$
$4\pi$	43008	1.14 min	7.24 s	20( $8.47 \times 10^{-9}$ )	$7.74 \times 10^{-7}$
$10\pi$	96768	5.93 min	1.02 min	48( $8.17 \times 10^{-9}$ )	$8.92 \times 10^{-7}$

## Acknowledgments

WL is partially supported by NSF of Zhejiang Province for Distinguished Young Scholars Grant LR21A010001, NSFC Grant 12174310, and a Key Project of Joint Funds For Regional Innovation and Development (U21A20425). The work of LX is supported by NSFC Grant 12071060. TY gratefully acknowledges support from NSFC through Grant 12171465.

## References

- [1] B. K. Alpert, Hybrid Gauss-trapezoidal quadrature rules, SIAM J. Sci. Comput. 20 (1999) 1551-1584.
- [2] T. Arens, T. Hohage, On radiation conditions for rough surface scattering problems, IMA J. Appl. Math. 70 (2005) 839-847.
- [3] G. Bao, G. Hu, T. Yin, Time-harmonic acoustic scattering from locally perturbed half-planes, SIAM J. Appl. Math. 78 (2018) 2672-2691.

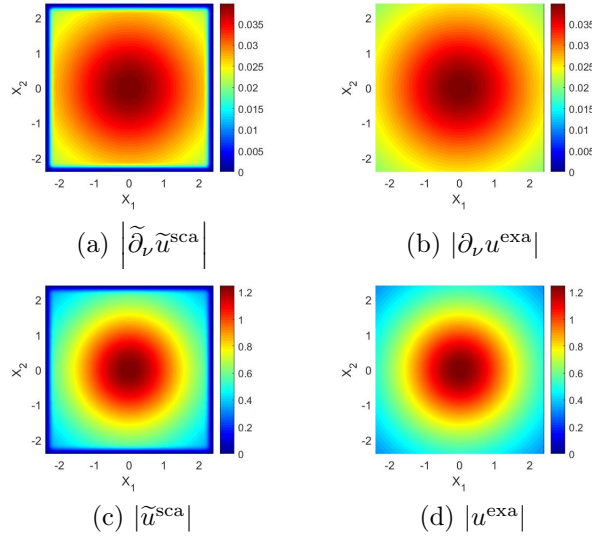


Figure 11: (a)(b): Absolute values of the  $\tilde{\partial}_\nu \tilde{u}^{\text{sca}}$  and  $\partial_\nu u^{\text{exa}}$  for the Dirichlet problem; (c)(d): Absolute values of the  $\tilde{u}^{\text{sca}}$  and  $u^{\text{exa}}$  for the Neumann problem. Here,  $k = 10\pi$ .

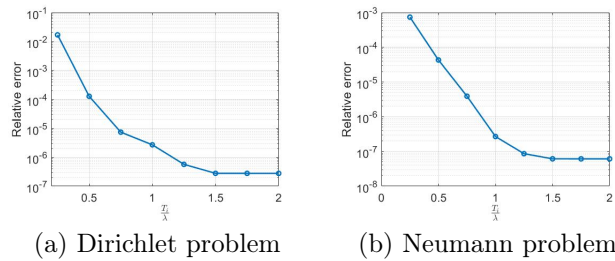


Figure 12: Numerical errors  $\epsilon_\infty$  with respect to  $\frac{T_l}{\lambda}$

- [4] G. Bao, J. Lin, Imaging of local surface displacement on an infinite ground plane: The multiple frequency case, *SIAM J. Appl. Math.* 71 (2011) 1733-1752.
- [5] G. Bao, L. Xu, T. Yin, An accurate boundary element method for the exterior elastic scattering problem in two dimensions, *J. Comput. Phys.* 348 (2017) 343-363.
- [6] G. Bao, L. Xu, T. Yin, Boundary integral equation methods for the elastic and thermoelastic waves in three dimensions, *Comput. Method Appl. Mechanics Eng.* 354 (2019) 464-486.
- [7] O. P. Bruno, B. Delourme, Rapidly convergent two-dimensional quasi-periodic Green function throughout the spectrum including wood anomalies, *J. Comput. Phys.* 262 (2014) 262-290.
- [8] O.P. Bruno, T. Elling, C. Turc, Regularized integral equations and fast high-order solvers for sound-hard acoustic scattering problems, *Int. J. Numer. Meth. Eng.* 91 (2012) 1045-1072.
- [9] O. P. Bruno, E. Garza, A Chebyshev-based rectangular-polar integral solver for scattering by general geometries described by non-overlapping patches, *J. Comput. Phys.* 421 (2020) 109740.
- [10] O. P. Bruno, E. Garza, C. Pérez-Arancibia, Windowed Green function method for nonuniform open-waveguide problems, *IEEE Trans. Antennas and Propagation.* 65 (2017) 4684-4692.



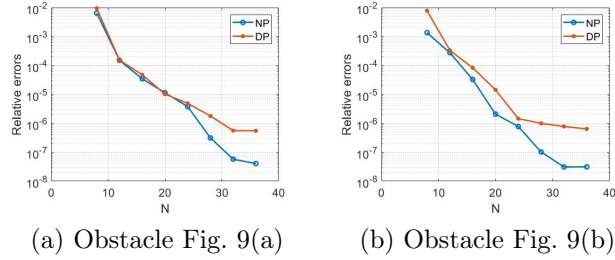


Figure 13: Numerical errors for the Dirichlet and Neumann problems of scattering by the obstacles given in Fig. 9(a-b) on the half-space. DP: Dirichlet problem, NP: Neumann problem

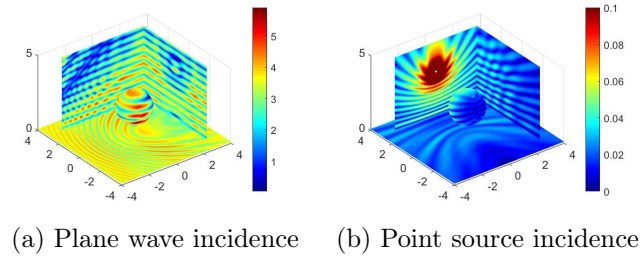


Figure 14: Absolute values of the total field resulting from the PML-based BIE method for the Neumann problem of scattering by the obstacle Fig. 9(a) on the half-space.

- [11] O. P. Bruno, M. Lyon, C. Pérez-Arancibia, C. Turc, Windowed Green function method for layered-media scattering, *SIAM J. Appl. Math.* 76 (2016) 1871-1898.
- [12] O. P. Bruno, C. Pérez-Arancibia, Windowed Green function method for the Helmholtz equation in presence of multiply layered media, *Proc. R. Soc. Lond. Ser. A Math. Phys. Eng. Sci.* 473 (2017) 20170161.
- [13] O. P. Bruno, T. Yin, Regularized integral equation methods for elastic scattering problems in three dimensions, *J. Comput. Phy.* 410 (2020) 109350.
- [14] O. P. Bruno, T. Yin, A windowed Green function method for elastic scattering problems on a half-space, *Comput. Methods Appl. Mech. Engrg.* 376 (2021) 113651.
- [15] W. Cai, Algorithmic issues for electromagnetic scattering in layered media: Green's functions, current basis, and fast solver, *Adv. Comput. Math.* 16 (2002) 157-174.

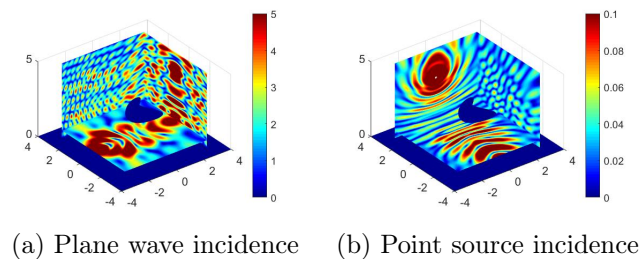


Figure 15: Absolute values of the total field resulting from the PML-based BIE method for the Dirichlet problem of scattering by the obstacle Fig. 9(c) on the half-space.

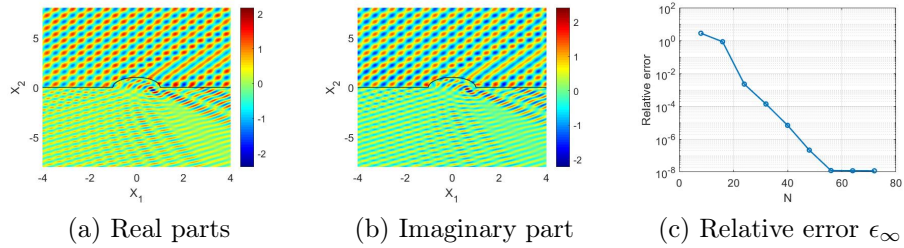


Figure 16: (a,b) Real and imaginary parts of the total fields by the PML-based BIE method for the problem of scattering of a plane-wave by a semicircular bump; (c) The relative error  $\epsilon_\infty$  of  $u^{\text{tot}}$  with respect to  $N$ .

- [16] S. N. Chandler-Wilde, B. Zhang, A uniqueness result for scattering by infinite rough surfaces, *SIAM J. Appl. Math.* 58 (1998) 1774-1790.
- [17] A. H. D. Cheng, T. Badmus, D.E. Beskos, Integral equation for dynamic poroelasticity in frequency domain with BEM solution, *J. Eng. Mech. Asce.* 117(5) (1991) 1136-1157.
- [18] W. C. Chew, *Waves and Fields in Inhomogeneous Media*, IEEE Press, New York, 1995.
- [19] W. C. Chew, W. H. Weedon, A 3D perfectly matched medium for modified Maxwell's equations with stretched coordinates, *Microw. Opt. Technol. Lett.* 7 (1994) 599-604.
- [20] S. Christiansen, J.C. Nédélec, A preconditioner for the electric field integral equation based on Calderón formulas, *SIAM J. Numer. Anal.* 40 (3) (2002) 1100-1135.
- [21] D. Colton, R. Kress, *Inverse Acoustic and Electromagnetic Scattering Theory*, Springer, Berlin, 1998.
- [22] J. DeSanto, P. A. Martin, On the derivation of boundary integral equations for scattering by an infinite one-dimensional rough surface, *J. Acoust. Soc. Am.* 102 (1997) 67-77.
- [23] Y. Gao, W. Lu, Wave scattering in layered orthotropic media I: a stable PML and a high-accuracy boundary integral equation method, *SIAM J. Sci. Comp.* 44 (2022) B861-B884.
- [24] G. C. Hsiao, W.L. Wendland, *Boundary Integral Equations*, Applied Mathematical Sciences, Vol.164, Springer-verlag, 2008.
- [25] R. Kittappa, R. E. Kleinman, Acoustic scattering by penetrable homogeneous objects, *J. Math. Phys.* 16 (1975) 421-432.
- [26] R. Kress, On the numerical solution of a hypersingular integral equation in scattering theory, *J. Comput. Appl Math.* 61 (1995) 345-360.
- [27] M. Lassas, E. Somersalo, Analysis of the PML equations in general convex geometry, *Proc. Roy. Soc. Edinburgh Sect. A.* 131 (2001) 1183-1207.
- [28] W. Lu, Mathematical analysis of wave radiation by a step-like surface, *SIAM J. on Applied. Math.* 81 (2021) 666-693.
- [29] W. Lu, G. Hu, Time-harmonic acoustic scattering from a nonlocally perturbed trapezoidal surface, *SIAM J. Sci. Comput.* 41 (2019) 522-544.
- [30] W. Lu, Y. Y. Lu, J. Qian, Perfectly matched layer boundary integral equation method for wave scattering in a layered medium, *SIAM J. Appl. Math.* 78 (2018) 246-265.

- [31] C. Macaskill, P. Cao, A new treatment of rough surface scattering, *Proc. R. Soc. Lond. A.* 452 (1996) 2593-2612.
- [32] A. W. Maue, Über die Formulierung eines allgemeinen Beugungsproblems durch eine Integraleichung, *Zeit. Physik.* 126 (1949) 601-618.
- [33] A. Meier, S. N. Chandler-Wilde, On the stability and convergence of the finite section method for integral equation formulations of rough surface scattering, *Math. Methods Appl. Sci.* 24 (2001) 209-232.
- [34] D. Miret, G. Soriano, M. Saillard, Rigorous simulations of microwave scattering from finite conductivity two-dimensional sea surfaces at low grazing angles, *IEEE Trans. Geosci. Remote Sensing.* 52 (2014) 3150-3158.
- [35] M. Paulus, P. Gay-Balmaz, O. Martin, Accurate and efficient computation of the Green's tensor for stratified media, *Phys. Rev. E.* 62 (2000) 5797-5807.
- [36] C. Pérez-Arancibia, O. P. Bruno, High-order integral equation methods for problems of scattering by bumps and cavities on half-planes, *J. Opt. Soc. Amer. A.* 31 (2014) 1738-1746.
- [37] M. Saillard, G. Soriano, Rough surface scattering at low-grazing incidence: A dedicated model, *Radio Sci.* 46 (2011) RS0E13.
- [38] P. Spiga, G. Soriano, M. Saillard, Scattering of electromagnetic waves from rough surfaces: A boundary integral method for low-grazing angles, *IEEE Trans. Antennas Propagation.* 56 (2008) 2043-2050.
- [39] L. Tsang, C. H. Chan, K. Pak, H. Sangani, Monte-Carlo simulations of large-scale problems of random rough surface scattering and applications to grazing incidence with the BMIA/canonical grid method, *IEEE Trans. Antennas Propagation.* 43 (2002) 851-859.
- [40] A. Willers, The Helmholtz equation in disturbed half-spaces, *Math. Methods Appl. Sci.* 9 (1987) 312-323.
- [41] T. Yin, G. C. Hsiao, L. Xu, Boundary integral equation methods for the two dimensional fluid-solid interaction problem, *SIAM J. Numer. Anal.* 55(5) (2017) 2361-2393.
- [42] X. Yu, G. Hu, W. Lu, A. Rathsfeld, PML and high-accuracy boundary integral equation solver for wave scattering by a locally defected periodic surface, *SIAM J. Numer. Anal.* 60 (2022) 2592-2625.
- [43] H. Zhang, B. zhang, A novel integral equation for scattering by locally rough surfaces and application to the inverse problem, *SIAM J. Appl. Math.* 73 (2013) 1811-1829.
- [44] L. Zhang, L. Xu, T. Yin, An accurate hypersingular boundary integral equation method for dynamic poroelasticity in two dimensions, *SIAM J. Sci. Comput.* 43 (2021) 784-810.
- [45] L. Zhang, L. Xu, T. Yin, Regularized hyper-singular boundary integral equation methods for three-dimensional poroelastic problems, *J. Comput. Phys.* 468 (2022) 111492.
- [46] Z. Zhao, L. Li, J. Smith, L. Carin, Analysis of scattering from very large three-dimensional rough surfaces using MLFMM and ray-based analyses, *IEEE Antennas Propagation Magazine.* 47 (2005) 20-30.